This article has been accepted for publication in IEEE Transactions on Applied Superconductivity. This is the author's version which has not been fully edited and content may change prior to final publication. Citation information: DOI 10.1109/TASC.2024.3495524

Design of a Novel Halbach Superconducting Geared Machine for an All-Electric Aircraft

Maurizio Marongiu, Alessandro Serpi, Alfonso Damiano, Andrea Floris

Abstract — The design of a novel configuration of an outer rotor, partially High Temperature Superconducting (HTS), magnetic geared synchronous machine for an All-Electric Aircraft (AEA) is presented in this paper. This is characterized by a three-phase inner stator with traditional windings and the use of HTS in the outer rotor instead of the permanent magnets in Halbach array configuration to generate the magnetization field. Moreover, the HTS is employed in the modulation ring instead of the ferromagnetic pole pieces to properly produce the flux modulation effect by exploiting the inherent feature of HTS of type II of having a magnetic permeability close to zero unless very intense magnetic fields are applied. This configuration is intended to be used as an electric motor for a light AEA equipped with 2 propellers of 200 kW each. The optimal configuration design has been obtained by resorting to an optimization procedure based on a genetic algorithm included in the finite element analysis software JMAG, complying with several targets and constraints, to satisfy a specific objective function. Performance analyses reveal the effectiveness of the proposed design configuration and approach, ensuring the compliance with all the design targets.

Index Terms — All-Electric Aircraft, Halbach effect, High temperature superconducting, Magnetic geared machine, Optimization design, Synchronous machine

I. INTRODUCTION

In 2022, the CO_2 emissions due to air transport have exceeded 800 Mt. This value represents the 2% of the overall CO_2 emissions and it is likely to increase in future years [1]. In order to solve this problem and remove the concern of generating harmful gas from fossil fuels, several solutions have been proposed that aim to implement more electrified technologies, such as the More Electric Aircraft (MEA) and the All-Electric Aircraft approach (AEA). In particular, thanks to the exclusive use of electric energy for supplying both propulsion and power systems, AEA is considered one of the most promising solutions. However, nowadays, AEA presents a critical issue related to energy sources, which do not exhibit adequate energy density. Available lithium-ion batteries present an energy density up to 0.2 kWh/kg, far from that of traditional fossil fuel (10 kWh/kg, [2]). For this reason, the electrification of aviation is focusing on the areas of MEA, light AEA, and AEA that usually do not require long-term and, thus, energy-intensive flights.

Focusing on the AEA propulsion systems, the employment of Electrical Machines (EMs) instead of fossil fuel-based engines guarantees not only emission reduction, but also making remarkably silent, light and efficient power trains, especially if advanced design solutions are implemented [3], [4]. Furthermore, strict reliability and safety requirements are set for EMs used in AEA applications. In particular, the EM must fail safely without deteriorating or causing damage to any other aircraft systems. Consequently, Induction EMs and Rotor Wound EMs should be considered because they are inherently fail-safe. However, these kinds of EMs are characterized by low specific power and relatively low efficiency [5]. In this regard, recent studies have set new standards regarding the performance of EMs to be employed in AEA, by imposing a limit for specific power higher than 5 kW/kg, with a rated efficiency higher than 98% [6], [7], [8]. These performance are very difficult to achieve by conventional EMs, which generally exhibit 0.5÷1 kW/kg [9]. Very promising solutions are represented by High-Speed Permanent Magnet Synchronous Machines (HS-PMSMs) and more innovative EM configurations, in which the flux modulation effect is implemented, such as the Vernier PMSMs. In particular, the latter take advantage from all the benefits of HS-PMSMs, by ensuring low-speed/high-torque outputs at the same time [10], [11]. This results in EMs with high specific power, torque density and efficiency. Furthermore, direct drive solutions can be achieved, by eliminating bulky and inefficient mechanical transmission systems. However, the high specific power requirement introduces several thermal challenges and constraints. This is critical especially for HS-PMSMs, due to the limited operating temperature of PMs, to not reach permanent demagnetization.

To get more benefits with less issues, for some time now, solutions based on the use of High-Temperature Superconducting (HTS) are under study for AEA [9], [11], [17]. As long as an operating temperature below the HTS critical one is kept, HTS exhibits an electric resistivity equal to zero. This allows reaching very high current density, magnetic flux density and magnetomotive force values than using Permanent Magnets (PMs) or traditional copper windings. Thanks to these advantages, HTS-based EMs achieve very low volume and weight and, consequently, high specific power, torque density and efficiency. Several HTS-based EMs configurations have been proposed in the literature, which can be roughly classified into fully and partially HTS topologies [5], [19]. The former is characterized by the use of the HTS in both the stator and the rotor and is generally employed in low-speed high-power EMs. The latter has HTS only in the rotor while the stator is

Maurizio Marongiu, Alessandro Serpi, Alfonso Damiano and Andrea Floris are with the Department of Electrical and Electronic Engineering of the University of Cagliari, Italy (andrea.floris86@unica.it)

This article has been accepted for publication in IEEE Transactions on Applied Superconductivity. This is the author's version which has not been fully edited and content may change prior to final publication. Citation information: DOI 10.1109/TASC.2024.3495524

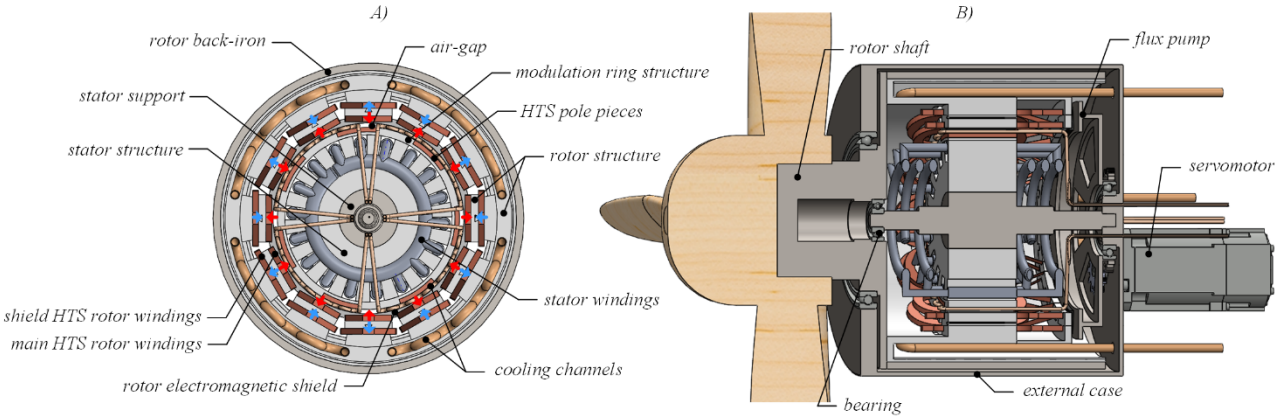

Fig. 1. Cross-sections of the proposed SMGM: plane view with rotor windings magnetization (A) and axial view (B).

characterized by the three-phase winding made up of traditional conductors. This solution is generally employed in high-speed EMs in which the use of HTS would lead to high AC losses due to high supply frequency. In other solutions, the HTS can be employed as bulk to replace the ferromagnetic pole pieces of magnetic gears or Vernier EMs [17]. This is due to an inherent feature of HTS of Type II materials (e.g. BSCCO, YBCO, and GdBCO), namely having a magnetic permeability close to zero unless very intense magnetic fields are applied. This feature prevents a large part of the magnetic field penetration in the bulk HTS [10], [18], [20].

In this context, the design of a novel configuration of an outer rotor, HTS Magnetic Geared synchronous Machine (SMGM) for an AEA is presented in this paper. This is a partially HTS-based EM, in which a novel Halbach HTS winding configuration has been employed to replace the Halbach PM array in the rotor. In this regard, two different windings, called main and shield HTS winding, have been considered. Moreover, to properly generate the flux modulation effect, a modulation ring with 7 HTS bulk has been employed in SMGM. Regarding the stator, 18 slots hosting a three-phase, one pole pair, and 3 slot per phase winding made up of Litz-wire conductors has been considered. The proposed SMGM is intended to be used as a direct-drive propulsion EM of a light AEA, consisting of 2 propellers of 200 kW each [21]. The optimal SMGM design has been obtained by resorting to an optimization procedure based on a genetic algorithm included in the Finite Element Analysis (FEA) software JMAG. In particular, several SMGM geometrical and operating parameters are set variable within appropriate ranges. Furthermore, several targets and constraints have been imposed in order to satisfy a specific objective function. The performance analysis reveals the effectiveness of the proposed design configuration and approach. Particularly, the proposed configuration complies with all design targets and constraints, by ensuring the expected performance as well [22].

The paper is structured as follows: a brief description of the proposed configuration and its operating principle are presented in Section II. Section III presents the SMGM electromagnetic modeling, based on which the FEA design procedure has been carried out (Section IV). The main parameters of the designed configuration are presented in Section V, together with extensive FEA results. The manuscript ends with some concluding remarks and future trends (Section VI).

II. Configuration and Operating Principle

The cross-section of the proposed SMGM configuration is reported in Fig. 1. It consists of different main components, such as an outer rotor with HTS windings, an inner stator with a traditional three-phase winding, and an HTS-based modulation ring interposed between them. The modulation ring is physically connected to the stator and the HTS pole pieces are embedded in the modulation ring structure. Since the rotor and the stator are characterized by different pole pairs numbers, the modulation ring has the task of modulating the magnetic field produced by the rotor and the stator windings. In this way, the interaction between them in the air-gap occurs as they would be characterized by the same number of pole pairs and speed value. This goal requires satisfying the following relationship:

$$p_r + p_s = n_p \tag{1}$$

in which p_r and p_s represent the rotor and stator pole pairs number, respectively, while n_p is the number of HTS pole pieces in the modulation ring. Consequently, the flux modulation effect occurs and the gear ratio G is defined as

$$G = \frac{p_r}{p_s} = \frac{\omega_s}{p_s \omega_r} = \frac{2\pi f_s}{p_s \omega_r} \tag{2}$$

where ω_r and ω_s represent the rotating mechanical speed of the rotor and the electrical speed of the stator magnetic field, respectively, while f_s is the supply frequency. From Fig. 2 to Fig. 5, the main SMGM components are highlighted separately and they will be explained in detail in the next subsections.

A. Rotor

The SMGM outer rotor highlighted in Fig. 2A and Fig. 2B has been preferred compared to inner rotor solutions because it guarantees the large space required to arrange the HTS windings, and facilitates the design and layout of the cooling system. This rotor is characterized by 6 pole pairs, and made up of two concentrated HTS windings, i.e. main and shield winding. The former is responsible for the magnetization field and actively participates in the electromechanical energy

This article has been accepted for publication in IEEE Transactions on Applied Superconductivity. This is the author's version which has not been fully edited and content may change prior to final publication. Citation information: DOI 10.1109/TASC.2024.3495524

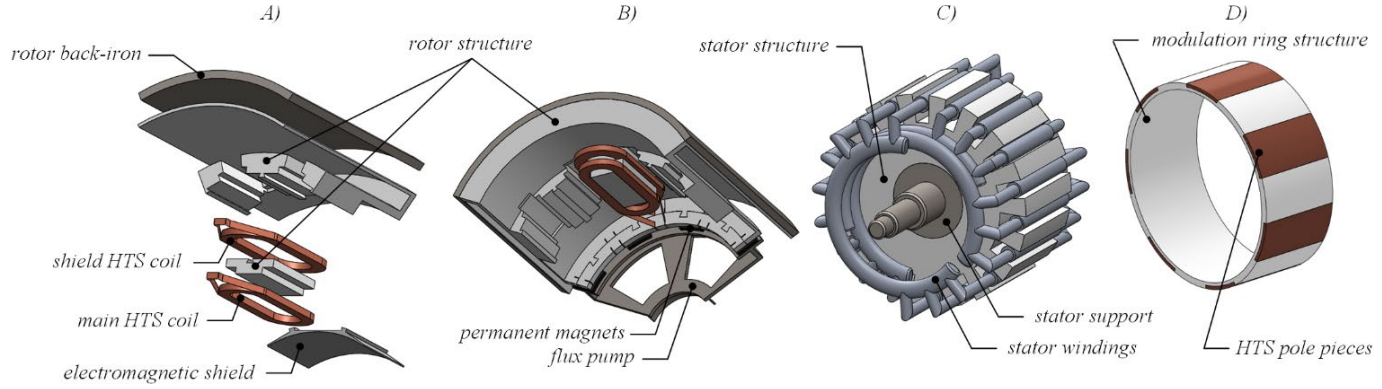

Fig. 2. View of the SMGM different components: A) rotor exploded view; B) rotor cross-section with the PM flux pump view; C) stator; D) modulation ring.

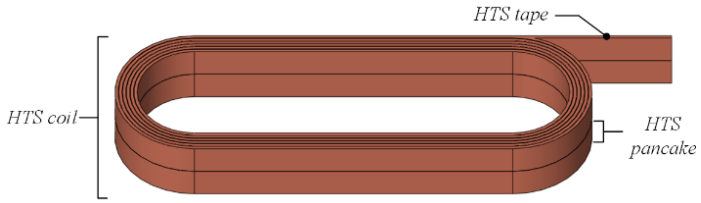

Fig. 3. Rotor HTS coil view.

TABLE I. SMGM MATERIAL PARAMETERS

Variable	Sym	Unit	Value
HTS tape (several materials + YBCO [24])			
Critical temperature	$T_{t,max}$	K	92
Tape cross-section	S_t	mm^2	0.445
Mass density	ρ_t	kg/m^3	8850
Minimum bend diameter	d_{tmax}	mm	10
HTS bulk (sterling YBCO [35])			
Critical temperature	$T_{b,max}$	K	92
Mass density	ρ_b	kg/m^3	6350
Cobalt-Iron alloy (VACOFLUX 50 [29])			
Mass density	ρ_i	kg/m^3	8120
Maximum magnetic flux density	$B_{i,max}$	T	2.2
Aluminum (series 6000 [27])			
Mass density	ρ_a	kg/m^3	2900
Thermal conducibility @40K	c_a	W/(mK)	300
Aluminum (series 1000 [32])			
Mass density	ρ_a	kg/m^3	2700
Electric resistivity @65K	γ_a	Ω/m	1.4e^{-9}
Composite glass fiber (G10 [26])			
Mass density	ρ_g	kg/m^3	1800
Thermal conducibility	c_g	W/(mK)	0.288
Mechanical strength	σ_g	MPa	310

Fig. 1.A), has the task of partially shielding the rotor back-iron from the magnetic flux density produced by the main HTS winding, concentrating it in the air-gap. This shielding effect is similar to that achievable by using the Halbach PM array [17], [23]. Both HTS windings are constituted by one HTS coil for each magnetic pole, as shown in Fig. 2A. Each HTS coil consists of one or more series-connected HTS pancakes, which are in turn made up of several HTS thin tapes, as shown in Fig. 3. The main characteristics of the HTS tape, characterized by several materials among which YBCO (Yttrium Barium Copper Oxide), are reported in Table I [24], [25]. The right combination of HTS tapes and pancakes should be chosen to optimize the SMGM performance suitably. Generally, each HTS coil is assembled by using particular winding machines and, subsequently, the coil with a race-track shape (Fig. 3) is placed in the rotor.

Given this HTS winding layout, the rotor structure has been designed as a novel modular structure of two components, as highlighted in Fig. 2A. This structure simplifies the HTS coil assembly phase. Both HTS windings are kept below the critical HTS temperature (< 92 K), guaranteeing an electrical resistance virtually equal to zero. Consequently, when a DC current flows in the HTS windings, no Joule losses occur, enabling the achievement of very high current density values (> 500 A/mm^2), not feasible by traditional windings. This results in a very high magnetizing current, which, however, could cause unwanted magnetic saturation phenomena and/or eddy current losses if ferromagnetic materials were employed for the rotor structure. Therefore, a Glass Fiber (G10 [26]) has been selected for the rotor structure, whose main properties are reported in Table I. This material guarantees a low overall weight due to the low mass density, and a good mechanical strength, which avoids mechanical failure at maximum speed operation. Furthermore, G10 exhibits a very high electric resistivity, even at cryogenic temperatures, thus successfully limiting the eddy current losses in the rotor due to the modulation effect. In this regard, other composite materials like carbon fiber are unsuitable due to the low electric resistivity at low temperatures [28].

A rotor electromagnetic shield made up of Aluminum (Series 6000 [27]) is also placed on the rotor surface that faces the air gap, as shown in Fig. 2A. It mainly consists of a cylinder that shields the HTS windings from any AC magnetic field produced by the stator winding. This effect occurs due to the eddy currents induced in the material, which oppose to the stator magnetic field and, thus, almost suppress its effect inside the rotor. In addition, the Aluminum electromagnetic shield increases the mechanical robustness of the rotor.

In conclusion, a thin rotor layer of Cobalt-Iron Alloy (VACOFLUX 50 [29]), which exhibits a maximum flux density value of approximately 2.2 T ($B_{i,max}$), is externally and coaxially arranged. This is employed to focus the magnetic flux paths that are not completely prevented by the HTS shield winding, thus

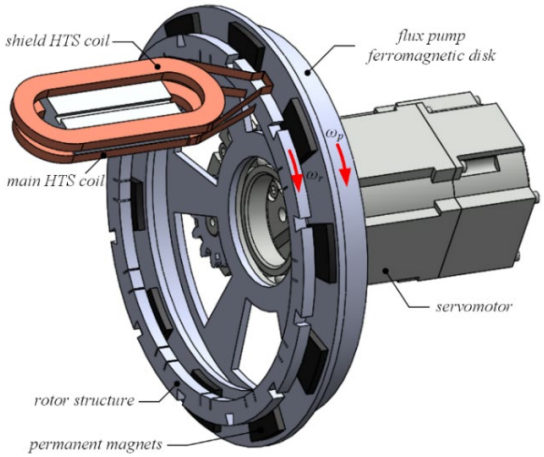

Fig. 4. PM flux pump view.

preventing an excessive magnetic flux leakage. In this way, a small increase in the mass and volume of the SMGM is achieved, but at the benefit of a large increase in torque density and specific power.

B. Flux pump

The current circulation in the HTS windings is guaranteed by a PM flux pump, rotor-coaxially arranged, as highlighted in Fig. 4. It consists of a ferromagnetic disk, with several PMs, driven by an electric servomotor, which could be connected to the PM disk either directly or through a mechanical gear. The latter solution enables the employment of a compact and lightweight high-speed servomotor, thus it may result in lower volume and weight compared to a direct drive solution.

Regarding the HTS flux pump, its working mechanism can be explained as follows. It is worth remembering that a non-linear resistivity characterizes the HTS material; this is the key and the only necessary characteristic of a material to be used in an HTS flux pump. Indeed, contrary to traditional conductive materials with linear resistivity, where the net voltage in one complete cycle is always zero, the accumulation of an induced electric field in the HTS tape results in a certain net DC voltage, which causes flux pumping [30]. Consequently, since the relative speed between the SMGM rotor and the flux pump ($\omega_r - \omega_p$) is kept different from zero, the varying magnetic field produced by the PMs induces a net DC voltage in the HTS windings and, consequently, a DC current different from zero [31]. It is worth noting that a high relative speed between the SMGM and the flux pump rotors is obtained only at the SMGM start-up, when the HTS rotor windings need to be magnetized. At steady state operation, this relative speed is rather low, together with the corresponding eddy currents induced in the HTS tapes.

C. Stator

The inner stator, shown in Fig. 2C, is characterized by a three-phase distributed traditional winding. Although the stator winding is not HTS-based, it is kept at a cryogenic temperature too. This allows for a great reduction of the electrical resistance in the winding and, consequently, the high current density can be obtained (> 20 A/mm^2) without incurring overtemperature phenomena due to Joule losses [16]. Consequently, light materials for the stator winding can be employed, such as Aluminum Series 1000 (Table I), which exhibits a lower electrical resistance than copper and other aluminum alloys at cryogenic temperature [32], [33]. Furthermore, round wires have been considered, which guarantee low AC winding losses at high-speed operation, especially when Litz-Wire with small cross-sections are employed [34].

Regarding the stator structure, since this hosts variable magnetic flux density with a high-frequency harmonic content, the glass fiber G10 already used for the rotor structure has been employed also in this case, because it is characterized by a high electrical resistivity and low magnetic permeability (Table I). Consequently, unwanted eddy currents and magnetic saturation phenomena are avoided.

D. Modulation ring

The modulation ring, highlighted in Fig. 2D, is made up of a suitable number of HTS pole pieces in accordance with (1), embedded in a glass fiber (G10) modulation ring structure. Each HTS pole piece consists of a thin bulk of sterling YBCO material, whose main characteristics are reported in Table I [35], [36]. As long as the HTS bulk works below the HTS critical temperature (< 92 K), it prevents a large part of the magnetic flux density penetration, emulating the flux modulation effect of the ferromagnetic pole pieces in the traditional magnetic gear. However, in SMGM, this effect is completely independent from the HTS bulk thickness. Thus, they can be fabricated with a very short thickness in radial direction, contributing to increasing SMGM specific power and torque density [10], [18].

E. Cooling system

To guarantee the cryogenic temperature in the HTS windings and bulk, a cryogenic cooling system with liquid hydrogen has been considered, as shown in Fig. 5. This is characterized by 4 cooling serpentine channels in the SMGM rotor cooling chamber and in the air-gap each.

The rotor cooling channels present a high section to ensure the cryogenic temperature in the HTS parts, especially in both main and shield windings. Since the G10 employed for the rotor structure is characterized by a low heat exchange coefficient, the geometry of the rotor structure has been designed appropriately to expose the HTS rotor windings to the cooling channels directly. Consequently the heat exchange due to forced convection is favored by exploiting the rotation of the rotor. The airgap channels lie on the modulation ring (Fig. 5) and cool the HTS bulks in the modulation ring and the stator windings, also supporting the rotor channels in cooling the HTS windings.

All cooling channels are made up of G10 and should be carefully isolated from SMGM active parts to avoid explosions. The rated power of the cooling system and the flow rate of the refrigerant fluid strictly depend on the SMGM overall losses, which include the Joule losses in the stator windings and the losses in the ferromagnetic parts.

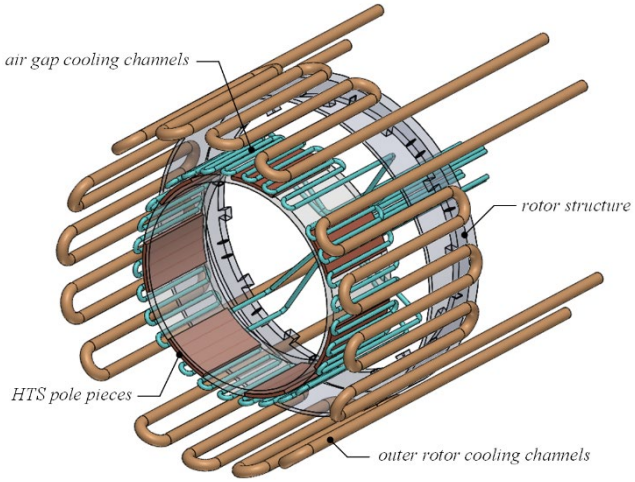

Fig. 5. Cooling channels view.

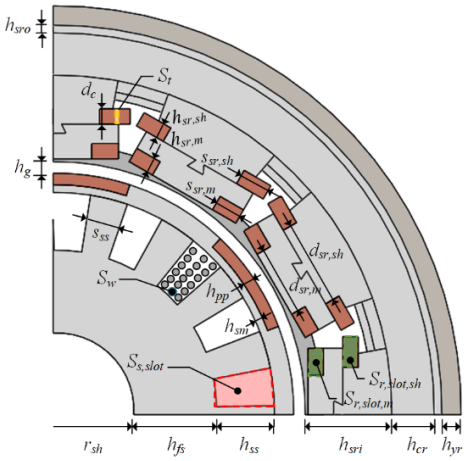

Fig. 6. SMGM cross-section with its main dimensions.

III. SMGM Modelling and Constraints

Each SMGM part must be designed taking into account different aspects carefully to reach all the imposed targets and constraints. In particular, the SMGM design must comply mainly with the maximum current density in the rotor and in the stator windings to avoid overheating due to excessive Joule losses. Moreover, the magnetic flux density and current values in the HTS rotor windings must be carefully evaluated to preserve the features of the HTS tape. Similarly, the maximum magnetic flux density achievable in the rotor back iron and in the air-gap must be evaluated to prevent magnetic saturation phenomena and guarantee the required EM performance, respectively [16].

Referring to the SMGM cross-section shown in Fig. 6, the rotor and stator current densities (J_r and J_s) depend on the rotor and stator slot area ($S_{r,slot}$ and $S_{s,slot}$,), on the HTS tape and stator wire cross-section (S_t and S_w), and on the number of series-connected HTS tapes and stator wires in each rotor and stator slot (N_t and N_w), respectively, leading to

$$J_{r/s} = I_{r/s,n} \frac{N_{t/w}}{S_{r/s,slot} F_{r/s}} \tag{3}$$

where $I_{s,n}$ is the stator rated phase current while $I_{r,n}$ is the rotor rated DC current, which must be kept always lower than the HTS critical value ($I_{HTS,max}$) to preserve the HTS features, as:

$$I_{r,n} < I_{HTS,\max} \tag{4}$$

in which $I_{HTS,max}$ is strictly dependent on HTS features, operating temperature and on maximum magnitude of the magnetic flux density perpendicular to the HTS tape ($B_{HTS,max}$), as highlighted in Fig. 7 [25]. Since the same PM flux pump is employed to excite main and shield HTS rotor windings, the same DC current value $I_{r,n}$ flows in both windings. Consequently, by assuming the same J_r for both rotor windings, $S_{r,slot}$ related to the main and the shield HTS coils ($S_{r,slot,m}$ and $S_{r,slot,sh}$, respectively) can assume a different value, due to a different number of HTS tapes that can make up the HTS coils ($N_{t,m}$, $N_{t,sh}$).

Still regarding (3), $F_{r/s}$ is the slot fill factor (in per unit) in the rotor and stator, respectively, which is expressed as:

$$F_{r/s} = \frac{S_{t/w} N_{t/w}}{S_{r/s,slot}} . \tag{5}$$

The rotor fill factor (F_r) can be very high, assuming a value close to 1, since a rectangular S_t is considered. In particular, S_t depends on the HTS tape thickness (s_{HTS}) and width (w_{HTS}) as

$$S_t = s_{HTS} \cdot w_{HTS} . \tag{6}$$

On the other hand, the stator fill factor (F_s) is assumed equal to 0.45, which represents a typical value when round wires are employed. Regarding S_w, it should be chosen suitably small in order to reduce the AC stator winding losses, including proximity and skin loss effects [33]. However, given a specific stator current value $I_{s,n}$, if S_w is too small, the current density in the stator wire can be too high, with a high probability of failure due to very high Joule losses.

Focusing now on the peak value of the magnetic flux density in the rotor back-iron (B_{yr}), a very good estimation can be obtained by resorting to FEA. The latter guarantees more accurate results than analytical models, which are also generally far from trivial [3], [37]. In order to avoid saturation phenomena, B_{yr} is imposed always lower than the magnetic saturation threshold of the iron material ($B_{i,max}$), leading to the following inequality:

$$B_{yr} \le B_{i,\max} . \tag{7}$$

The maximum value of B_{yr} can be reduced by increasing the rotor back-iron thickness [38]. However, a large back-iron increases the SMGM volume and weight, reducing its specific power and torque density unsuitably. Accordingly, the smallest possible back iron thickness is recommended.

Considering now the magnetic flux density in the air-gap achieved by FEA (B_g), it can be associated to the pressure that generally occurs in a turbo-jet engine (25÷40 atm), which

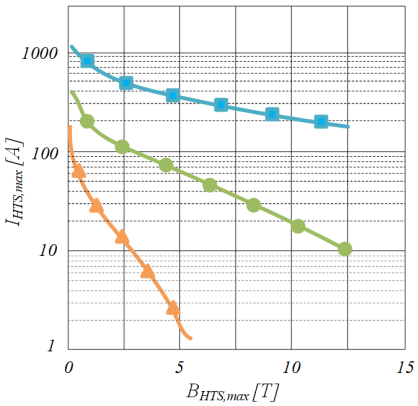

Fig. 7. YBCO maximum current values at different magnetic flux density values at different operating temperatures: 40 K (blue curve with squares), 65 K (green curve with circles), and 77 K (orange curve with triangles) [25].

provides an indication of the machine's energy density. In this regard, the following empirical inequality must be satisfied:

$$B_g > \sqrt{\frac{P}{4}}. \tag{8}$$

Consequently, a B_g value higher than 2.5-3 T should be achieved to comply with the target specific power (> 5 kW/kg) [16], [22].

Other electromagnetic aspects regard the evaluation of the overall losses. In particular, the following inequality must be satisfied in order to comply with the efficiency target (>98%):

$$P_{e,loss} = P_j + P_i < P_n \cdot 0.02 \tag{9}$$

in which $P_{e,loss}$ represents the overall electromagnetic losses in the SMGM at rated operating condition, while P_j and P_i are the Joule losses in the stator winding and the losses in the ferromagnetic parts, at the same conditions, respectively, both computed by FEA. In conclusion, SMGM torque ripple is constrained to avoid excessive vibration and noise [4]:

$$T_{ripple} = \frac{T_{\max} - T_{\min}}{T_n} < T_{r,\lim} \tag{10}$$

in which T_{max} and T_{min} are the maximum and minimum torque values at rated operating conditions, while T_n is the corresponding average torque and $T_{r,lim}$ is the maximum allowable torque ripple (in per unit), which, in this case, is imposed equal to 0.15.

IV. SMGM Design

A. Design specifications and constant parameters

The main design specifications and constant parameters of the SMGM presented in this paper are reported in Table II. In particular, the proposed SMGM should be characterized by a rated power and outer speed equal to 200 kW and 2500 rpm, respectively. Consequently, the SMGM rated torque is set at approximately 760 Nm. These values have been chosen by considering the turbofan engine size generally employed in light airplanes characterized by 2-6 seats [21]. The maximum

TABLE II. SMGM Design Specifications and Constant Parameters

Parameter	Sym	Unit	Value
Stator			
Operating temperature	t_{sn}	K	65
Slot numbers	$n_{s,slot}$	-	18
Pole pair numbers	p_s	-	1
Slot fill factor	F_s	-	0.45
Rated supply frequency	f_s	Hz	250
DC-link voltage	V_{DC}	V	500
Tooth width	s_{ss}	mm	10
Structure thickness	h_{fs}	mm	10
Rotor			
Operating temperature	t_{rn}	K	40
Output rated speed	$\omega_{r,n}$	rpm	2500
Output maximum speed	$\omega_{r,max}$	rpm	5000
Air-gap	h_g	mm	5
Slot fill factor	F_r	-	1
Pole pair numbers	p_r	-	6
Current density	J_r	A/mm^2	500
Rated current	$I_{r,n}$	A	222
HTS tape cross-section	S_t	mm^2	0.445
Outer structure thickness	h_{rso}	mm	4
Colling channels chamber thickness	h_{cr}	mm	10
Modulation ring			
Operating temperature	t_{mn}	K	40
HTS pole piece numbers	N_p	-	7
HTS pole-pieces thickness	h_{pp}	mm	5
Structure thickness	h_{sm}	mm	2

SMGM outer speed is set equal to 5000 rpm in accordance with the characteristics of the propeller. In particular, the latter is characterized by a radial length of 0.47 m, and a maximum peripheral speed of 250 m/s.

The SMGM inner stator is characterized by 2 poles, 18 slots and 3 slots per pole per phase. On the other hand, the SMGM rotor is made up of 12 poles, and its rated speed (2500 rpm) also represents the propeller rotational speed. To guarantee the transmission of a constant torque, 7 HTS bulks in the modulation ring with a thickness of 5 mm are considered, by satisfying (1). This results in a magnetic gear ratio (G) equal to 6. Consequently, the range of the supply frequency is set at 250-500 Hz, while the DC-link voltage has been set at 500 V in accordance with typical values occurring and foreseeing for this application. Regarding the HTS rotor windings, a current density equal to 500 A/mm^2 is imposed. Consequently, by considering an HTS tape characterized by a standard cross-section (S_t) of 0.445 mm^2 [25], a rated current value in the HTS tape equal to 222 A is obtained. The SMGM operating temperature is assumed equal to 40 K in the rotor and in the modulation ring, and to approximately 65 K in the stator, guaranteeing a good safety margin from the HTS critical temperature. In these conditions, considering Fig. 7, the HTS windings can maintain the superconducting state up to a magnetic flux density value ($B_{t,max}$) equal to 10 T. The air-gap and the thickness of the cooling chamber are set equal to 5 mm and 10 mm, respectively, guaranteeing enough space for the cooling channels placement.

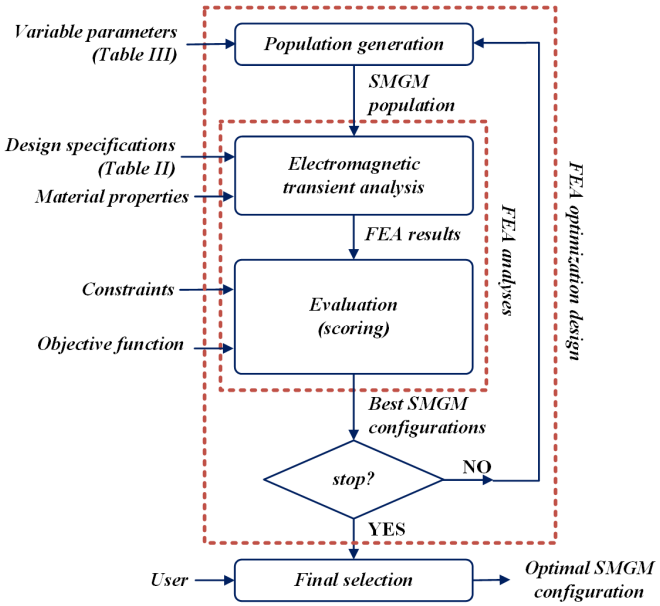

Fig. 8. Workflow of the SMGM FEA design procedure.

TABLE III. SMGM VARIABLE PARAMETERS

Variable	Sym	Unit	Range
Axial active length	L	mm	10÷500
Stator			
Shaf radius	r_{sh}	mm	10÷100
Slot height	h_{ss}	mm	2÷30
Rated phase current	$I_{s,n}$	A	100÷1000
Current density	J_s	A/mm^2	10÷45
Rotor			
Back-iron thickness	h_{yr}	mm	2÷100
HTS main winding tooth width	$d_{sr,m}$	mm	20÷30
HTS shield winding tooth width	$d_{sr,sh}$	mm	20÷60
Radial distance between HTS main and shield coils	d_c	mm	10÷40
HTS main winging pancake number	N_{p_m}	-	1÷7
HTS shield winging pancake number	N_{p_sh}	-	1÷7

B. FEA design procedure

The workflow of the design procedure employed in this paper is shown in Fig. 8. It is based on FEA and a Genetic Algorithm (GA) embedded into the FEA software JMAG. The FEA design procedure starts from a number of variable parameters that vary within appropriate operating ranges, as reported in Table III. In this regard, it is worth noting that the lower limit for the rotor tooth widths ($d_{sr,m/sh}$) is set at 20 mm by considering the maximum HTS tape curvature radius to avoid tape breakages [25]. Consequently, a first SMGM casual population is obtained, which undergoes a transient electromagnetic analysis in accordance with design specifications (Table II) and material properties. Once FEA results have been achieved, which include the main electromagnetic machine performance, SMGM population is scored accordingly, by considering all constraints reported in Section III and a given objective function, which, in this case, is the maximization of the specific power. The best SMGM configurations of the current

TABLE IV. SMGM MAIN PARAMETERS

Parameter	Sym	Unit	Value
Rated torque	T_n	Nm	753.5
Rated power	P_n	kW	197.3
Rated speed	$\omega_{m,n}$	rpm	2500
Overall active volume	V	dm^3	12.3
Overall active weight	M	kg	29.1
Specific power	SP	kW/kg	6.9
Torque density	TD	kNm/m^3	61.3
Axial active length	L	mm	101.5
Stator			
Shaft radius	r_{sh}	mm	80
Slot height	h_{ss}	mm	13.1
Rated phase current	$I_{s,n}$	A	378
Current density	J_s	A/mm^2	25.6
Wire turns for slots	N_w	-	23
Slot area	$S_{s,slot}$	mm^2	25.6
Wire cross-section	S_w	mm^2	6.65
Rotor			
Back-iron thickness	h_{yr}	mm	10.6
HTS main winding tooth width	$d_{sr,m}$	mm	22.5
HTS shield winding tooth width	$d_{sr,sh}$	mm	47.7
HTS main winging pancake number	N_{p_m}	-	4
HTS shield winging pancake number	N_{p_sh}	-	1
HTS main winging tape number	N_{t_m}	-	575
HTS shield winging tape number	N_{t_sh}	-	114
Radial distance between HTS main and shield winding	d_c	mm	18.6

population are thus obtained and, if the GA stopping criterion is not met, a new generation of SMGM population is setup accordingly, and the procedure is repeated iteratively. When the GA stopping criterion is satisfied (i.e. the maximum number of generations in this case), the user selects the optimal SMGM configuration manually among the best SMGM configurations belonging to the last generation.

In conclusion, it is worth noting that the maximum number of generations, as well as the population size for each generation and the number of best SMGM configurations have been set to 30, 100, and 10, respectively.

V. RESULTS

The main parameters of the proposed SMGM together with its rated values are summed up in Table IV, while the main electromagnetic FEA results are reported in Table V. In particular, the overall SMGM volume and weight are 12.3 dm^3 and 29.1 kg, respectively. It is worth noting that these values are comprehensive of the active SMGM parts and do not include the components that do not take part in the energy conversion. As a result, by considering a rated power and torque of 197.3 kW and 753.55 Nm, respectively, a specific power of 6.9 kW/kg and a torque density of 61.3 kNm/m^3 are obtained, by complying with the design targets. Referring to the stator phase windings, an aluminum wire cross-section of 6.65 mm^2 and a maximum current density of 25.6 A/mm^2 have been obtained, respectively. Hence, a configuration of 23 turns per slot has been achieved. This results in a slot area of 340 mm^2

This article has been accepted for publication in IEEE Transactions on Applied Superconductivity. This is the author's version which has not been fully edited and content may change prior to final publication. Citation information: DOI 10.1109/TASC.2024.3495524

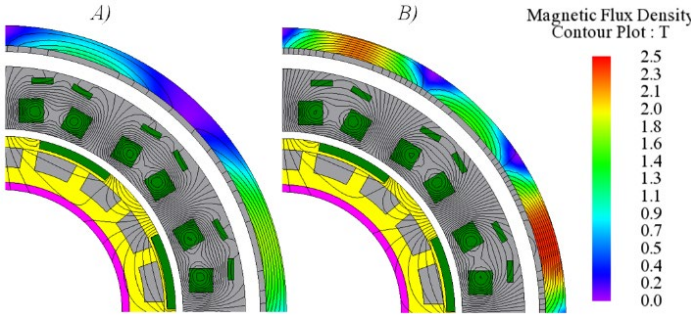

Fig. 9. Stator open circuit magnetic flux density distribution of the designed SMGM: $I_{r,sh} = I_{r,n}$ (A), $I_{r,sh} = 0$ (B).

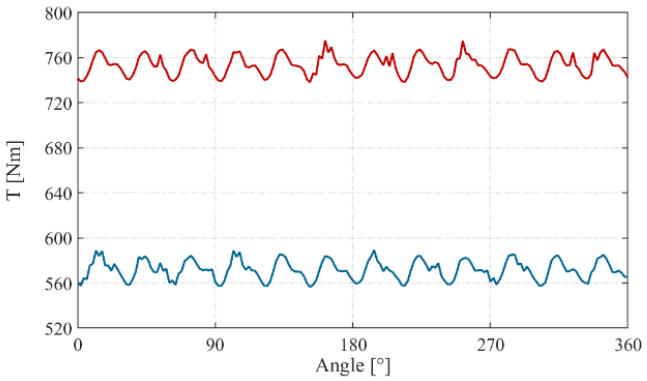

Fig. 10. Torque evolution at rated operating conditions of the designed SMGM: with rotor back iron (in red); without rotor back iron (in blue).

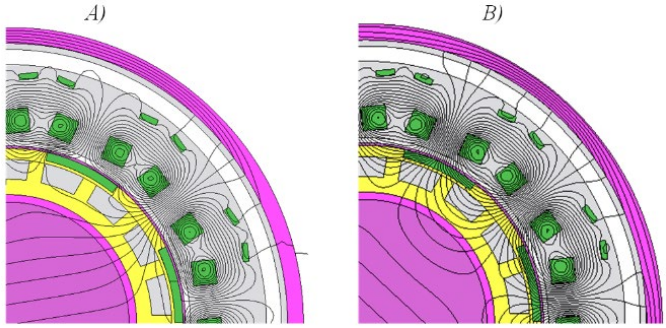

Fig. 11. Rated condition magnetic flux lines of the designed SMGM: modulation ring with HTS pole pieces (A), modulation ring with ferromagnetic pole pieces (B).

TABLE V. SMGM FEA RESULTS*

Parameter	Sym	Unit	Value
Torque ripple	T_{ripple}	%	4.9
Back-emf magnitude	E	V	370
Max Rotor back-iron magnetic flux density	B_{yr}	T	2.1
Max Rotor structure magnetic flux density	B_{sr}	T	3.5
Max air-gap magnetic flux density	B_g	T	4.5
Iron losses	P_i	W	191.8
Joule losses	P_j	W	2997
Efficiency	η	%	98.4

**at rated operating conditions*

by assuming a slot fill factor of 0.45. Regarding the rotor HTS windings, they are characterized by 575 and 114 tapes for the main and shield windings, which are arranged in 4 and 1 pancakes, respectively. This ensures the required electromagnetic performance, by concentrating the magnetic flux density produced by the main winding towards the air-gap, shielding the rotor back-iron at the same time. Consequently, a relatively small rotor back-iron thickness is achieved (10.6 mm); this aspect is well highlighted in Fig. 9, which shows the stator open-circuit distribution of the magnetic flux density in the rotor back-iron. In particular, Fig. 9A highlights the distribution of B_{yr} when the Halbach effect is achieved due to the DC current flowing in the HTS main and shield windings, whereas Fig. 9B shows the distribution of B_{yr} with no current flowing through the HTS shield winding ($I_{r,sh} = 0$). It can be seen that a maximum B_{yr} value of 1.7 T is achieved in the first case (Fig. 9A), by complying with (7), whereas a maximum B_{yr} value of 2.5 T would be achieved without the shielding effect (Fig. 9B), which would have overcome the saturation threshold of the iron material.

Regarding torque evolution, an average output torque value of about 753 Nm is obtained (Fig. 10), with a ripple torque lower than 5%, thus satisfying (10). This torque evolution has been obtained at rated conditions, by imposing sinusoidal three-phase stator currents with a peak value of 378 A and a frequency of 250 Hz. Fig. 10 also shows the torque evolution in case of no back-iron, which reveals an average value significantly lower than that achieved in the previous case (from 753 Nm to 571 Nm), thus not complying with the design specifications. This is because the magnetic flux density due to HTS rotor main winding is not completely shielded by the HTS shield winding. Consequently, although eliminating the rotor back iron would reduce SMGM weight and volume significantly, this guarantees a preferential path for the residual magnetic flux density, increasing the SMGM torque capability. As a result, an SMGM with rotor back iron ensures higher torque density and specific power compared to the other solution.

The very good electromagnetic results previously presented and discussed are achieved thanks to the magnetic modulation effect due to the HTS bulks in the modulations ring, which ensure high torque density and specific power. This aspect is highlighted in Fig. 11, which shows the distribution of the magnetic flux lines at the rated condition of the designed SMGM. In particular, Fig. 11A shows the designed configuration, in which the pole pieces in the modulation ring are constituted by HTS bulks. At the same time, Fig. 11B highlights the same configuration but considers a hypothetical case in which the pole pieces are made up of ferromagnetic material (VACOFLUX 50). It can be noted that the ferromagnetic pole pieces (Fig. 11 B), characterized by a high magnetic permeability material and a thickness of 5 mm, are unable to provide a preferential path for the magnetic flux lines, with a consequent poor modulation effect and a low rated average torque equal to 150 Nm. Contrariwise, due to a magnetic permeability close to zero, the HTS pole pieces (Fig. 11 A), with the same thickness, guarantee an almost perfect magnetic modulation effect, achieving, consequently, the desired performance.

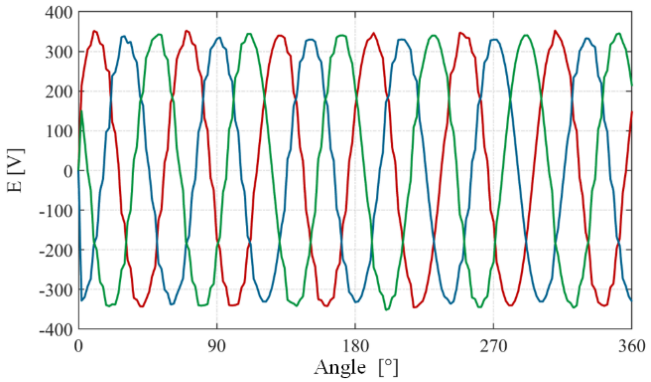

Fig. 12. Back-emf evolution of the designed SMGM at rated operating conditions.

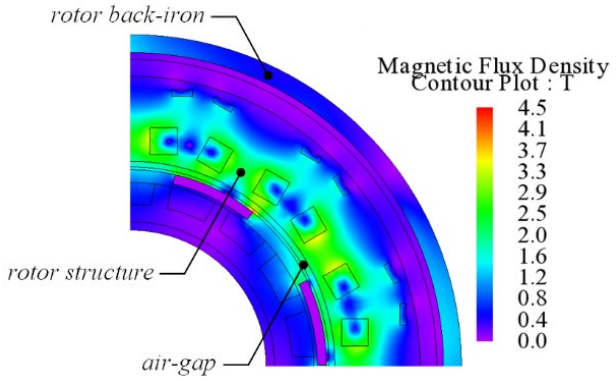

Fig. 13. Magnetic flux density distribution of the designed SMGM at rated operating conditions.

Moreover, the evolution of the back-emfs in the three-phase winding, shown in Fig. 12, exhibits a fairly good sinusoidal shape, with a magnitude of approximately 350 V. Furthermore, the distribution of magnetic flux density at rated operating conditions in the different SMGM parts is highlighted in Fig. 13; it can be seen that all maximum values in the different SMGM parts comply with (7) and (8), with a maximum value of 4.5 T in the air-gap. In conclusion, as resumed in Table V, the proposed SMGM presents very low overall losses, which results in a very high efficiency at rated conditions (98.4%), even greater than that required by (9).

VI. Conclusion

In this paper, the design and optimization of a novel configuration of an outer rotor, high temperature Superconducting, Magnetic Geared synchronous Machine (SMGM) are presented. This is characterized by a three-phase inner stator with traditional winding and the use of HTS in the outer rotor to produce the magnetization field, instead of an Halbach array permanent magnets arrangement. Moreover, the HTS is employed in the modulation ring in place of the ferromagnetic pole pieces to properly modulate the magnetic flux by exploiting the features of the HTS material. The proposed configuration is intended to be employed as a propulsion motor for a light All Electric Aircraft (AEA) consisting of 2 propellers of 200 kW each. The optimal SMGM design has been obtained by resorting to an optimization procedure based on a genetic algorithm embedded into the Finite Element Analysis (FEA) software JMAG. The FEA results have demonstrated that the design solutions proposed in the paper enables high specific power and torque density, as well as energy efficiency, making the proposed SMGM suitable for AEA applications

VII. References

[1] International Energy Agent, 'CO2 Emissions in 2022'. Accessed: Aug. 23, 2023. [Online]. Available: https://www.iea.org/energy-system/transport/aviation

[2] J. Benzaquen, J. He, and B. Mirafzal, 'Toward more electric powertrains in aircraft: Technical challenges and advancements', *Trans. Electr. Mach. Syst.*, vol. 5, no. 3, pp. 177–193, Sep. 2021, doi: 10.30941/CESTEMS.2021.00022.

[3] A. Damiano, A. Floris, G. Fois, I. Marongiu, M. Porru, and A. Serpi, 'Design of a High-Speed Ferrite-Based Brushless DC Machine for Electric Vehicles', *IEEE Transactions on Industry Applications*, vol. 53, no. 5, pp. 4279–4287, Sep. 2017.

[4] E. Brescia, M. Palmieri, G. L. Cascella, and F. Cupertino, 'Optimal Tooth Tips Design for Cogging Torque Suppression of Permanent Magnet Machines with a Segmented Stator Core', in *2020 International Conference on Electrical Machines (ICEM)*, Aug. 2020, pp. 1930–1936. doi: 10.1109/ICEM49940.2020.9270968.

[5] E. Sayed *et al.*, 'Review of Electric Machines in More-/Hybrid-/Turbo-Electric Aircraft', *IEEE Transactions on Transportation Electrification*, vol. 7, no. 4, pp. 2976–3005, Dec. 2021, doi: 10.1109/TTE.2021.3089605.

[6] R. Jansen, G. V. Brown, J. L. Felder, and K. P. Duffy, 'Turboelectric Aircraft Drive Key Performance Parameters and Functional Requirements', in *51st AIAA/SAE/ASEE Joint Propulsion Conference*, Orlando, FL: American Institute of Aeronautics and Astronautics, Jul. 2015. doi: 10.2514/6.2015-3890.

[7] A. EL-Refaie and M. Osama, 'High Specific Power Electrical Machines: A System Perspective'.

[8] J. Zhao, X. Zhang, N. Swaminathan, and K. S. Haran, 'An Overview of High Specific Power Electrical Machines and Drives Technologies for Electrified Aircraft', in *2022 IEEE Energy Conversion Congress and Exposition (ECCE)*, Detroit, MI, USA: IEEE, Oct. 2022, pp. 1–8. doi: 10.1109/ECCE50734.2022.9948102.

[9] X. Zhang, C. L. Bowman, T. C. O'Connell, and K. S. Haran, 'Large electric machines for aircraft electric propulsion', *IET Electric Power Applications*, vol. 12, no. 6, pp. 767–779, Jul. 2018, doi: 10.1049/iet-epa.2017.0639.

[10] Chunhua Liu, K. T. Chau, Jin Zhong, Wenlong Li, and Fuhua Li, 'Quantitative Comparison of Double-Stator Permanent Magnet Vernier Machines With and Without HTS Bulks', *IEEE Trans. Appl. Supercond.*, vol. 22, no. 3, pp. 5202405–5202405, Jun. 2012, doi: 10.1109/TASC.2011.2180870.

[11] K. Chen and B. Sarlioglu, 'Vernier Machine Analysis and Analytical Design for Traction Applications', in *2021 International Aegean Conference on Electrical Machines and Power Electronics (ACEMP) & 2021 International Conference on Optimization of Electrical and Electronic Equipment (OPTIM)*, Brasov, Romania: IEEE, Sep. 2021, pp. 426–431. doi: 10.1109/OPTIM-ACEMP50812.2021.9590078.

[12] S. S. Kalsi, J. G. Storey, J. M. Brooks, G. Lumsden, and R. A. Badcock, 'Superconducting Synchronous Motor Development for Airplane Applications - Mechanical and Electrical Design of a Prototype 100 kW Motor', *IEEE Trans. Appl. Supercond.*, vol. 33, no. 5, pp. 1–6, Aug. 2023, doi: 10.1109/TASC.2023.3242629.

[13] P. J. Masson and C. A. Luongo, 'HTS Machines for Applications in All-Electric Aircraft', in *2007 IEEE Power Engineering Society General Meeting*, Tampa, FL, USA: IEEE, Jun. 2007, pp. 1–6. doi: 10.1109/PES.2007.385622.

[14] P. J. Masson and C. A. Luongo, 'High Power Density Superconducting Motor for All-Electric Aircraft Propulsion', *IEEE Trans. Appl. Supercond.*, vol. 15, no. 2, pp. 2226–2229, Jun. 2005, doi: 10.1109/TASC.2005.849618.

[15] M. Filipenko *et al.*, 'Concept design of a high power superconducting generator for future hybrid-electric aircraft', *Supercond. Sci. Technol.*, vol. 33, no. 5, p. 054002, May 2020, doi: 10.1088/1361-6668/ab695a.

[16] G. V. Brown *et al.*, 'NASA Glenn Research Center Program in High Power Density Motors for Aeropropulsion', 2005.
[17] T. Tymosch, M. Fischer, V. Ketchedjian, Y. Terao, and H. Ohsaki, 'Analysis of Superconducting Synchronous Motors With Halbach Array Field Excitation', *IEEE Trans. Appl. Supercond.*, vol. 31, no. 2, pp. 1–5, Mar. 2021, doi: 10.1109/TASC.2020.3041314.
[18] Linni Jian, K. T. Chau, Wenlong Li, and Jiangui Li, 'A Novel Coaxial Magnetic Gear Using Bulk HTS for Industrial Applications', *IEEE Trans. Appl. Supercond.*, vol. 20, no. 3, pp. 981–984, Jun. 2010, doi: 10.1109/TASC.2010.2040609.
[19] L. H. Zheng, J. X. Jin, Y. G. Guo, and J. G. Zhu, 'Technical and Theoretical Analysis of HTS Machines and Their Development'.
[20] N. Arish, F. Marignetti, and M. Yazdani-Asrami, 'Comparative study of a new structure of HTS-bulk axial flux-switching machine', *Physica C: Superconductivity and its Applications*, vol. 584, p. 1353854, May 2021, doi: 10.1016/j.physc.2021.1353854.
[21] *SENECA V PA-34-220T Pilot's Operating Handbook*.
[22] R. Jansen, G. V. Brown, J. L. Felder, and K. P. Duffy, 'Turboelectric Aircraft Drive Key Performance Parameters and Functional Requirements', in *51st AIAA/SAE/ASEE Joint Propulsion Conference*, Orlando, FL: American Institute of Aeronautics and Astronautics, Jul. 2015. doi: 10.2514/6.2015-3890.
[23] D. C. Loder and K. S. Haran, 'Multi-objective optimization of an actively shielded superconducting field winding: Pole count study', in *2015 IEEE International Electric Machines & Drives Conference (IEMDC)*, Coeur d'Alene, ID: IEEE, May 2015, pp. 1709–1714. doi: 10.1109/IEMDC.2015.7409294.
[24] A. Molodyk *et al.*, 'OPEN Development and large volume production of extremely high current density -YBa2Cu3O7 superconducting wires for fusion', *Scientific Reports*.
[25] Faraday Factory, 'Japan LLC HTS tape'. Accessed: Sep. 06, 2023. [Online]. Available: https://www.faradaygroup.com/en/product/
[26] Laminated Plastics, 'Technical Data Sheet G-10'. Accessed: Nov. 27, 2023. [Online]. Available: https://laminatedplastics.com/g-10.pdf
[27] MatWeb Material Properties Data, 'Aluminum Series 6000 Alloy'. Accessed: Nov. 27, 2023. [Online]. Available: https://www.matweb.com/search/datasheet.aspx?MatGUID=26d19f2d20654a489aefc0d9c247cebf&ckck=1
[28] Y. Wang, I. Ramos, R. Furlan, and J. J. Santiago-Aviles, 'Electronic Transport Properties of IncipientGraphitic Domains Formation in PAN Derived Carbon Nanofibers', *IEEE Trans. Nanotechnology*, vol. 3, no. 1, pp. 80–85, Mar. 2004, doi: 10.1109/TNANO.2004.824036.
[29] VACUUMSCHMELZE, 'Flyer VACOFLUX 50'. [Online]. Available: https://vacuumschmelze.com/03_Documents/Brochures/Flyer%20VACOFLUX%2050.pdf
[30] A. Ghabeli, E. Pardo, and M. Kapolka, '3D modeling of a superconducting dynamo-type flux pump', *Sci Rep*, vol. 11, no. 1, Art. no. 1, May 2021, doi: 10.1038/s41598-021-89596-4.
[31] K. Hamilton, A. E. Pantoja, J. G. Storey, Z. Jiang, R. A. Badcock, and C. W. Bumby, 'Design and Performance of a "Squirrel-Cage" Dynamo-Type HTS Flux Pump', *IEEE Trans. Appl. Supercond.*, vol. 28, no. 4, pp. 1–5, Jun. 2018, doi: 10.1109/TASC.2018.2805161.
[32] MatWeb Material Properties Data, 'Aluminum Series 1000'. Accessed: Nov. 27, 2023. [Online]. Available: https://www.matweb.com/search/datasheet.aspx?matguid=38e1c167c7ea4dfebf80778b29ae71cf&ckck=1
[33] C. D. Manolopoulos, M. F. Iacchetti, A. C. Smith, P. Miller, and M. Husband, 'Litz wire loss performance and optimization for cryogenic windings', *IET Electric Power Appl*, vol. 17, no. 4, pp. 487–498, Apr. 2023, doi: 10.1049/elp2.12279.
[34] S. Li, Y. Li, W. Choi, and B. Sarlioglu, 'High-Speed Electric Machines: Challenges and Design Considerations', *IEEE Trans. Transp. Electrific.*, vol. 2, no. 1, pp. 2–13, Mar. 2016, doi: 10.1109/TTE.2016.2523879.
[35] I. Grekhov *et al.*, 'Growth mode study of ultrathin HTSC YBCO films on YBaCuNbO buffer', *Physica C: Superconductivity*, vol. 324, no. 1, pp. 39–46, Oct. 1999, doi: 10.1016/S0921-4534(99)00423-2.
[36] M. K. Wu *et al.*, 'Superconductivity at 93 K in a new mixed-phase Y-Ba-Cu-O compound system at ambient pressure', *Phys. Rev. Lett.*, vol. 58, no. 9, pp. 908–910, Mar. 1987, doi: 10.1103/PhysRevLett.58.908.
[37] A. Floris, A. Serpi, A. Damiano, and I. Hahn, 'Torque Harmonics Minimization of Double-Stage Magnetic Gear Transmission System', in *IECON 2019 - 45th Annual Conference of the IEEE Industrial Electronics Society*, Oct. 2019, pp. 2751–2757. doi: 10.1109/IECON.2019.8926636.
[38] J. R. Hendershot and T. J. E. Miller, *Design of brushless permanent-magnet machines*. Venice, Florida: Motor Design Books, 2010.

VIII. BIOGRAPHY

Maurizio Marongiu received the bachelor's degree in Electrical, Electronics and Computer Engineering from the University of Cagliari, Italy, in 2023, with the thesis entitled "Develop of a tool for the design of squirrel cage induction machines". In the same year, he won a research scholarship that regards the design and development of superconducting synchronous electrical machines to be used in power systems and aircraft propulsion systems. Maurizio Marongiu is currently a master's degree student in Energy engineering in the University of Cagliari, Italy.

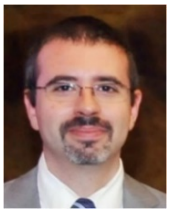

Alessandro Serpi (Member, IEEE) received the master's degree in electrical engineering and the Ph.D. in industrial engineering at the University of Cagliari, Italy, in 2004 and 2009, respectively. From 2016 to 2021 he was Assistant Professor at the Department of Electrical and Electronic Engineering of the same university, where he is now Associate Professor. Prof. Serpi is also co-founder, Chief Executive and Technology Officer of NEPSY srl, an academic spin-off company dealing with novel and highly integrated electric propulsion systems. He is co-author of approximately 100 papers published in international conference proceedings and journals. His research activity focuses on management, design and control of electrical machines, drives and energy storage systems. Prof. Serpi is a reviewer for several international conferences and journals. He received three IEEE award

Alfonso Damiano (Senior Member, IEEE) received the master's degree in electrical engineering from the University of Cagliari, Italy, in 1992. In 1994, he joined the Department of Electrical and Electronic Engineering of the same university as an Assistant Professor, where he became Associate Professor (from 2001 to 2018) and, then Full Professor (since 2018) of electrical machines and energy management. He has co-authored more than 170 papers published in international conference proceedings and journals. His current research interests include multiphase and high-speed electrical machines and drives, management and control of electric vehicles, and energy storage systems. Prof. Damiano is a reviewer for several international conferences and journals. He received an IEEE Paper Award.

Andrea Floris (Member, IEEE) received the bachelor's degree in mechanical engineering, and the master's degree in energy engineering from the University of Cagliari, Italy, in 2012 and 2015, respectively. In 2020 he received the Ph.D degree in electronic and computer engineering at the same university. Dr. Floris is currently Assistant Professor at the Department of Electrical and Electronic Engineering of the same university. He is co-author of 24 papers published in international conference proceedings and journals. His research activity regards the design of high-speed electrical machines, flywheel energy storage systems and magnetic gear transmission systems for electric vehicles. He received an IEEE Best Poster Presentation Award.